Physica Medica 67 (2019) 155–165

Contents lists available at ScienceDirect

Physica Medica

journal homepage: www.elsevier.com/locate/ejmp

Original paper

Variable tilt-angle, parallel-hole collimation system for high-resolution molecular imaging gamma tomosynthesis

Mariaconcetta Longo[a,*], Roberto Pani[b], Rosanna Pellegrini[c,d], Maria Nerina Cinti[c,d], Viviana Frantellizzi[e], Giuseppe De Vincentis[e]

[a] Sapienza University of Rome, Ph. D. Program in Morphogenesis & Tissue Engineering, Rome, Italy
[b] Department of Radiological Sciences, Oncology and Anatomical Pathology, Sapienza University of Rome, Rome, Italy
[c] Department of Molecular Medicine, Sapienza University of Rome, Rome, Italy
[d] INFN Roma I Section, Rome, Italy
[e] Department of Sciences and Medical and Surgical Biotechnologies, Sapienza University of Rome, Rome, Italy

ARTICLE INFO

Keywords:
Variable angle collimator
Molecular imaging
Image reconstruction
Small lesion detection
SPECT

ABSTRACT

Purpose: This study investigates a novel gamma tomosynthesis (GT) method based on a variable tilt-angle, parallel-hole collimator (VAPHC) which, mounting to a conventional gamma, is able to perform high-resolution three-dimensional imaging.

Methods: The VAPHC has the remarkable feature to be modular, consisting of independent collimation elements able to tilt according to variable angles [−45° to +45°]. Spatial resolutions were measured in reconstructed GT images using a point source at different source-to-collimator distances, while sensitivity was evaluated over the range of slant angles using a disk-source. Image contrast (IC) and contrast-to-noise-ratio (CNR) of sub-centimeters tumors were evaluated using a breast phantom containing a background activity and spheres filled with ^{99m}Tc to simulate lesions at two depths. Breast phantom GT images were compared with planar and circular-orbit SPECT acquisitions of equal scan-time.

Results: Planar spatial resolutions range from 9 to 14 mm over a depth range of 6–10 cm; spatial resolution in depth dimension becomes two times greater than those in the other dimensions. The measured sensitivity decreases from 9 cps/μCi to 6 cps/μCi varying the slant angle from 5° to 45°. The measured IC and CNR of GT reconstructed images demonstrated that it was possible to improve the spatial resolution/sensitivity trade-off.

Conclusions: The proposed GT based VAPHC demonstrated the potential for superior spatial resolution and contrast compared to planar and SPECT acquisitions. A conventional gamma camera equipped with the VAPHC could be located at the minimum distance from the patient, thus improving detection, localisation and characterisation of sub-centimetre lesions.

1. Introduction

The single-photon emission computed tomography (SPECT) technique is based on photon detection emitted by a radiotracer injected into the patient's body. In a traditional SPECT system, the acquisition is performed by collecting projection images one at time by stepwise rotating the gamma camera around the patient. Over the last few years, major improvements in SPECT systems have mainly been due to progress in terms of industrial processes regarding analogical electronic, crystal growing or photomultipliers tubes (PMTs) manufacturing [1–6]. Despite these improvements, SPECT systems are still characterised by poorer spatial resolution caused by object-to-detector distance, given by the detector orbiting motion, which also impairs efficiency and image quality. The still limited spatial resolution of conventional SPECT systems, which are large, bulky and designed for general-purpose imaging, is not ideal for small lesion imaging [7]. It is well known that the simplest way to improve spatial resolution capabilities is to reduce the patient-to-collimator distance. Recent advances in SPECT instrumentation and collimation systems have made marked improvements in this area, thus giving evident advantages in small lesion detection capabilities needed for early stage diseases.

In the last years, several image acquisition methods have been proposed. Some of these methods are based on fixed angle collimation systems: the acquisition is employed by acquiring a number of projections of the object while the detector moves in a circular orbit; sectional images are produced by a summation of filtered projections.

* Corresponding author.
E-mail address: longo.mariaconcetta@gmail.com (M. Longo).

https://doi.org/10.1016/j.ejmp.2019.10.028
Received 14 June 2019; Received in revised form 30 September 2019; Accepted 13 October 2019
Available online 08 November 2019

Ectomography represents a fixed angle collimators tomographic technique based on tomosynthesis [8]. Differently from SPECT, the direction of the projection is not in the plane of the section, but forms an angle with it, resulting in two-dimensional projections. The projections represent a widespread region, making it possible to image several sections. Another proposed rotational system is the Rotating Multi-Segment Slant-Hole (RMSSH) single photon emission computed tomography that finds its application in scintimammography [9]. The RMSSH system combines a conventional SPECT system with a RMSSH collimator. It is suitable for detecting small and low-contrast breast lesions since it boasts much higher detection efficiency than conventional SPECT with a parallel-hole collimator and can image the breast at a closer distance [9]. A fixed-angle collimator design may not permit optimisation of both collimator positioning (allowing the detector to be placed as close as possible to an object) and view angle, thus a variable angle collimation system could represent the only strategy to resolve these issues.

The idea of using variable angle collimators comes from 1983 when Moore et al [10] designed a Variable Angle Slant Hole (VASH) collimator. To improve the relationship of the collimator to the object, while maintaining the desired view, they built a prototype that permits the angle of slant to be easily adjusted by the operator. The collimator was composed of a series of tungsten plates that can be “sheared”, as with stacked decks of cards, to adjust the angle of view. However, this design suffered some limitations due to faulty registration of the plates at high angles of shear, where registration becomes more critical because of potential septal penetration and irregularity of hole shape. Following the same idea regarding the collimator movement Gopan et al. [11], by means of theoretical analysis and Monte Carlo simulation studies, evaluated the imaging performance of the VASH collimator, including the spatial resolution/sensitivity trade-off, compared with parallel-hole SPECT. The Monte Carlo studies were used to validate the theoretical analysis and to evaluate the imaging performance of the VASH collimator with a simulated breast phantom. A more recent study evaluated the VASH collimator performances through experimental measurements [12].

In the present study, the authors propose a variable tilt-angle, parallel-hole collimator (VAPHC) prototype which allows to implement an innovative detection system in nuclear medicine, which we will refer to as gamma tomosynthesis (GT). The VAPHC is able to tilt its holes through a completely new rotation system. Rather than rotate the camera around the patient, the detection device is located in a fixed position, at a minimum distance from the patient, improving spatial resolution capabilities especially in the detection of small lesions. The proposed device is able to acquire planar projection images at different angles, which are then arranged together through the Shift And Add (SAA) method in order to obtain the three-dimensional reconstruction of the studied object. Our previous work analyzed the effectiveness of the collimator prototype through Monte Carlo simulations and experimental measurements [13] with point sources and small field of view (FOV) gamma camera. The goal of the present study was to evaluate sensitivity, spatial resolution and imaging potentials of the VAPHC with a clinical gamma camera.

2. Materials and methods

2.1. The variable tilt-angle parallel-hole collimator

Differently from other collimators proposed in literature, the VAPHC has the remarkable feature to be modular, consisting of independent collimation elements joined together in the rotation movement [14]. It is constructed by a stack of collimation blocks, each containing an identical array of holes (Fig. 1). Each block is 25 mm high with 1.5 mm hexagonal holes, whilst the septal thickness is 0.2 mm. The holes are arranged in a close-packed hexagonal array to maximize the exposed area of detector surface. The total collimation area of $60 \times 100\,mm^2$ is enclosed in a $158 \times 168 \times 46\,mm^3$ case which can be directly placed on the gamma camera crystal that provides the resting base for the collimator. Therefore, empty spaces of 5 mm and 16 mm remain between the collimation blocks and the lower and upper sides of the collimator case respectively. The collimation elements are tilted towards the longest dimension of the aluminum frame. In one of the side faces (i.e., the $158 \times 46\,mm^2$) there are two guide slots for the bearings of rotation (Fig. 1(a)). Two semi-circular slots on the shortest sides of the case allow for collimator rotation, while two horizontal slots present in one of the two shortest sides serve to slide the ball bearings provided for the rotation. In Fig. 1(b) the components of a single collimation element are shown: a lead collimation element, two bronze plates (0.2 mm thick) and a lead plate (0.5 mm thick). Each collimation module is a bronze plate/lead plate/collimation element/bronze plate sandwich (Fig. 1(c)). The bronze plates serve to reduce the friction between the collimation elements during rotation, while the lead plate provides a shield between one element and the adjacent one; the lead plate is placed between a bronze plate and the collimation element (Fig. 1(d)). The lead plate has been introduced as the single collimation bar has discontinuous sides caused by the cut. On one hand, the lead plate prevents the presence of non-collimated areas that can be caused by the union of two collimation bar with not-smooth sides. On the other hand, the presence of these passive elements between the collimation modules could induce blockage of gammas causing count loss in the projection images. The entire collimation system is composed of five collimation modules (Fig. 1(e)).

The parallel-hole configuration is created by vertically aligning the collimation elements. During the rotation, each collimation element is in contact with the adjacent one, filling the space between the collimator case and the collimator’s bottom, which is empty in the parallel-hole collimator configuration. The two push blocks with sliding piston and the ball bearings assembled on the short sides of each collimation element allow mechanical translation during rotation. The slant configuration is created by tilting the collimation elements through the above-mentioned mechanism (Fig. 2(a)). The pivot axes of the collimator modules move to keep the modules flush with one another, varying the collimator slant angle continuously from -45° to $+45^\circ$. The tilting movement occurs in one dimension only, creating a variable slant-hole configuration within the x-y plane. The collimations system can be moved through a screw that allows either manual or automatic rotation by its connection to a stepper motor.

2.2. Acquisition and reconstruction method

The proposed device is able to acquire planar projection images at different angles that can then be arranged together in order to obtain the three-dimensional reconstruction of the studied object. This acquisition mode works similarly to what happens in digital X-ray tomosynthesis [16,17]. The reconstruction method is generally quite simple, consisting of the shifting and adding of the constituent projection images to bring structures of a given plane into registration, or focus [18]. Traditional SAA method is a fundamental analytic reconstruction algorithm to line up each image based on its shifting amount to generate reconstruction slices at specified depths [19]. This allows to emphasise structures in the in-focus plane and blurring out structures in other planes. This method, validated in a previous publication [13], will be applied in this work in order to perform the volumetric reconstruction of a studied object.

If z represents the source-to-detector distance, for n projection images, the amount of shift $s_k(z)$ necessary to bring objects in plane into focus for each collimation angle θ_k is

$$s_k(z) = \pm z \cdot \tan\theta_k \quad (1)$$

which is negative for negative θ_k and positive for positive θ_k, while k is the index that varies along the number of projections n. Moreover, with a small collimation system as the one proposed, a further shift S of the

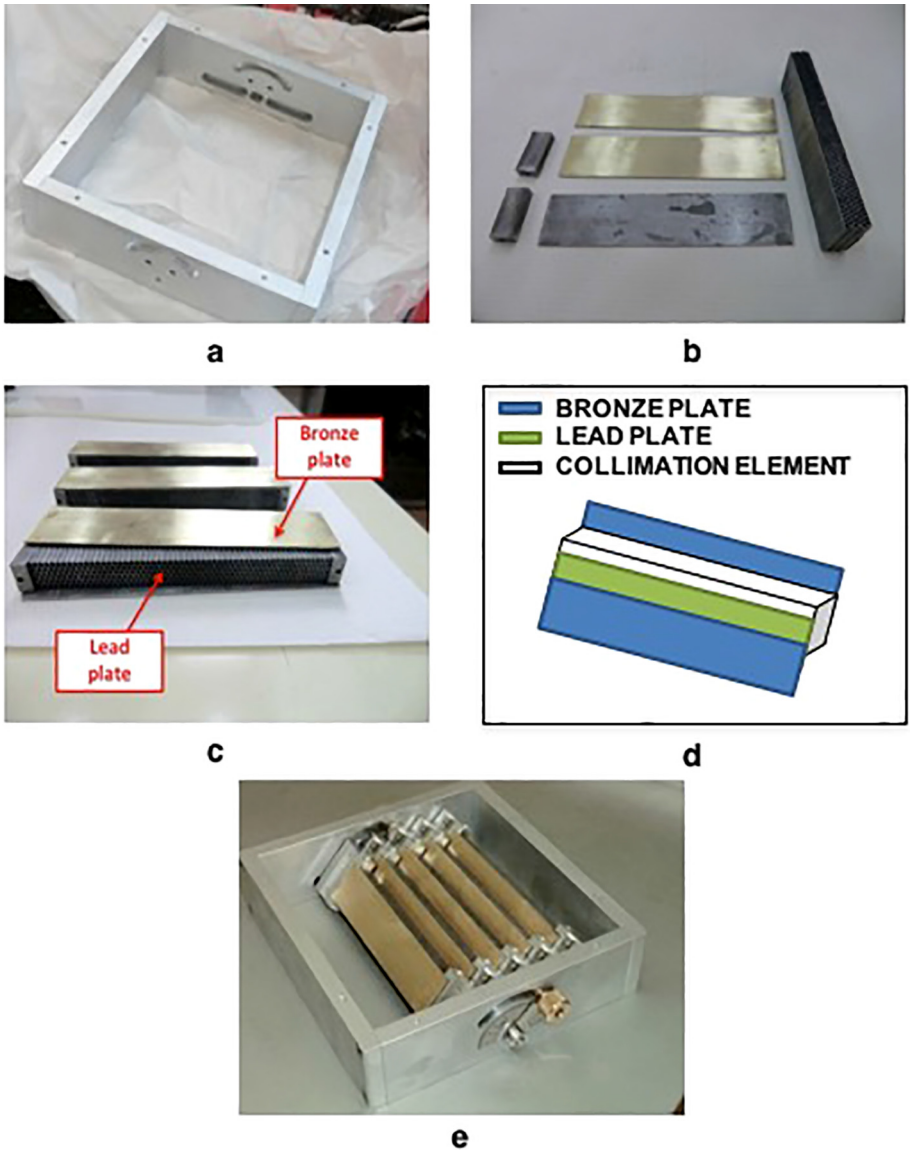

Fig. 1. Variable tilt-angle, parallel-hole collimation system. The collimator is produced by Kay Systems Italia S.P.A [15].

collimator along x direction has to be provided to guarantee the imaging of the entire object for all slant angles (Fig. 2(b)). In this case, the Eq. (1) becomes:

$$s_k(z) = -(z\cdot\tan\theta_k + S) \text{for negative} \theta_k$$
$$s_k(z) = +(z\cdot\tan\theta_k + S) \text{for positive } \theta_k \quad (2)$$

A tomosynthesis image $T_z(x',y')$ focalised in the plane at height z is the sum of all n shifted projection images convoluted by the Dirac delta function $\delta[x' - s_k(z)]$

$$T_z(x', y') = \sum_k I_k(x', y') * \delta[x' - s_k(z)] \quad (3)$$

where $I_k(x',y')$ are the acquired projection images and $s_k(z)$ is given by Eq. (2).

By using the impulse function's sifting property, all projection images are shifted by the proper amount. Therefore, with prior knowledge of the angle at which the projection is taken, and depending on the height of the reconstruction plane, each pixel is shifted by an appropriate amount.

2.3. Simulation

Before defining a set-up suitable for clinical application, some simulations were performed in order to test the contrast behavior as a function of the source's dimension and of the tumor to background ratio (TBR). The Monte Carlo simulations, based on GEANT4 toolkit, reproduced the variable slant hole collimator as a stack of lead elements (density 11.3 g/cm^3). The collimator has hexagonal-shaped holes with hole length of 25 mm, hole width of 1.5 mm and septal thickness of 0.2 mm. A continuous collimator (without bronze and lead plates) with a collimator sensitivity of 528 cpm/μCi was simulated. The simulated scintillation crystal was a 15 × 10 cm^2 NaI(Tl) scintillation crystal (density 3.67 g/cm^3), 6 mm thick, with a 0.2 mm thick Teflon tape for crystal wrapping in order to optimize light collection. A scintillation light yield equal to 38,000 photons/MeV was assumed for NaI(Tl). In addition, a light guide was coupled to the crystal, while a photo-detection surface was modeled as a polished SiO_2 3 mm thick glass window. The optical properties of the materials involved in the simulations (refraction index of 1.47, absorption lengths of 420 cm) were gathered from literature. To take into account photocathode quantum efficiency and Photo Multiplier Tube (PMT) anode pad, the number of light photons was reduced by an appropriate factor (24.5%). As ^{99m}Tc is

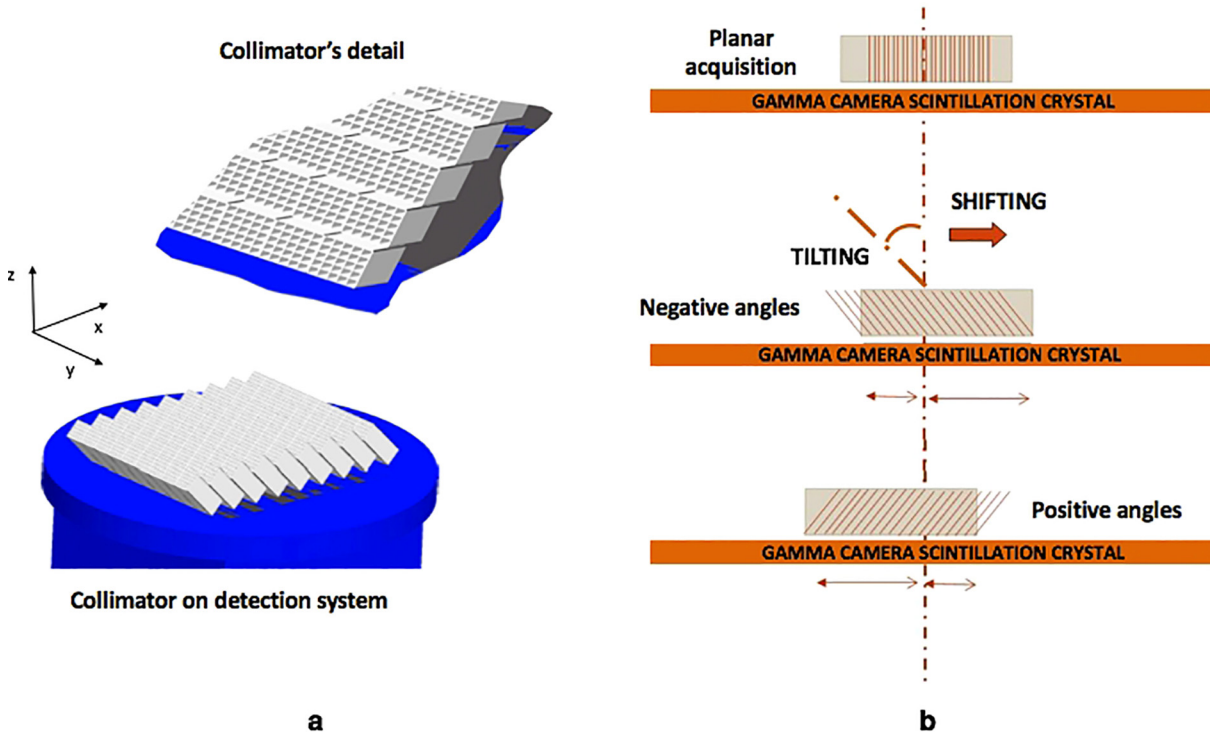

Fig. 2. Schematic views of the collimator's tilting mechanism. The schemes are not scaled.

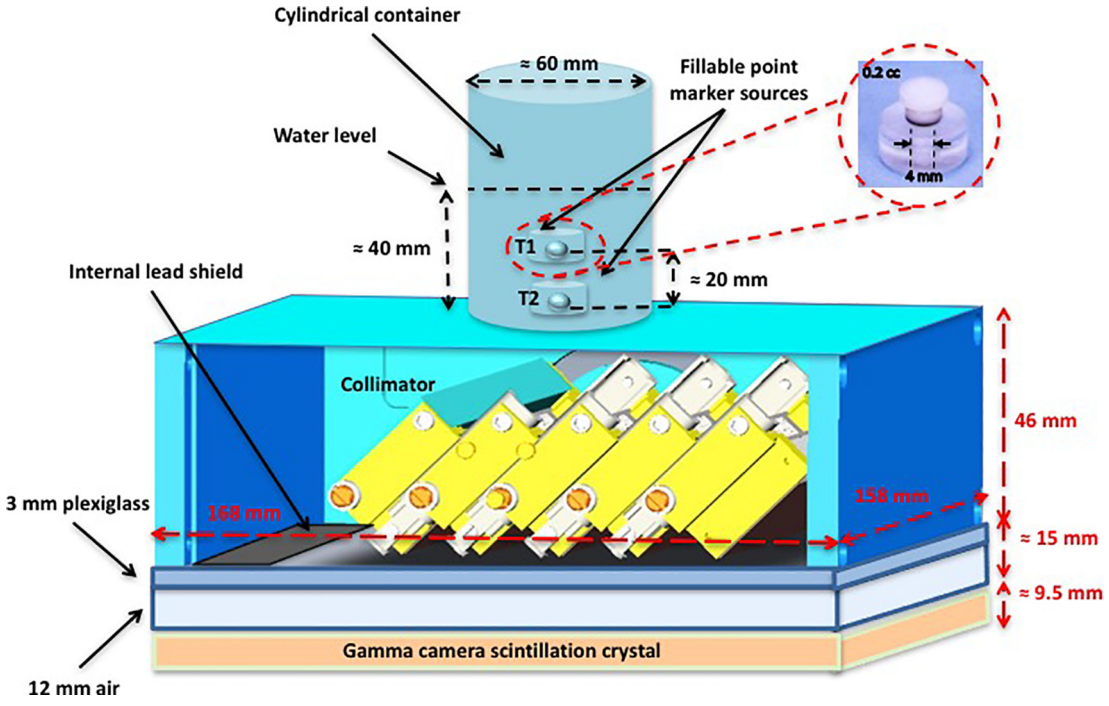

Fig. 3. Side view of the experimental set-up employed with breast phantom. The schemes are not scaled.

the most common radioisotope used in SPECT applications, 140 keV photon energy was used in the simulation. The electromagnetic processes were simulated, including low energy Rayleigh interactions and standard photoelectric and Compton interactions, in the object, collimator and scintillator. The phantom was realized as a cylindrical container, whose dimensions are compatible with those of a typical human organ, i.e. for example the breast. The cylinder was defined with a radius of 7.5 cm and height of 10 cm as suggest by Phelps [20]. The phantom contains two spherical hot spots, representing cancer lesions, with different diameters (5 mm and 10 mm respectively). To reproduce different TBR, the simulated activities for background and tumors were: 100 nCi/cc for the cylinder, 1 μCi/cc for the 10 mm sphere (TBR, 10:1), while several TBR (10:1, 15:1, 20:1, 30:1) were realized for the 5 mm sphere. The activity levels in the phantom, which well approximates a breast phantom, were representative of clinical Sestamibi breast imaging with an injected dose of 25 mCi, which results in breast activity concentrations from 38 nCi/ml to 176 nCi/ml [21]. Background and tumor images were separately simulated so that the final images were

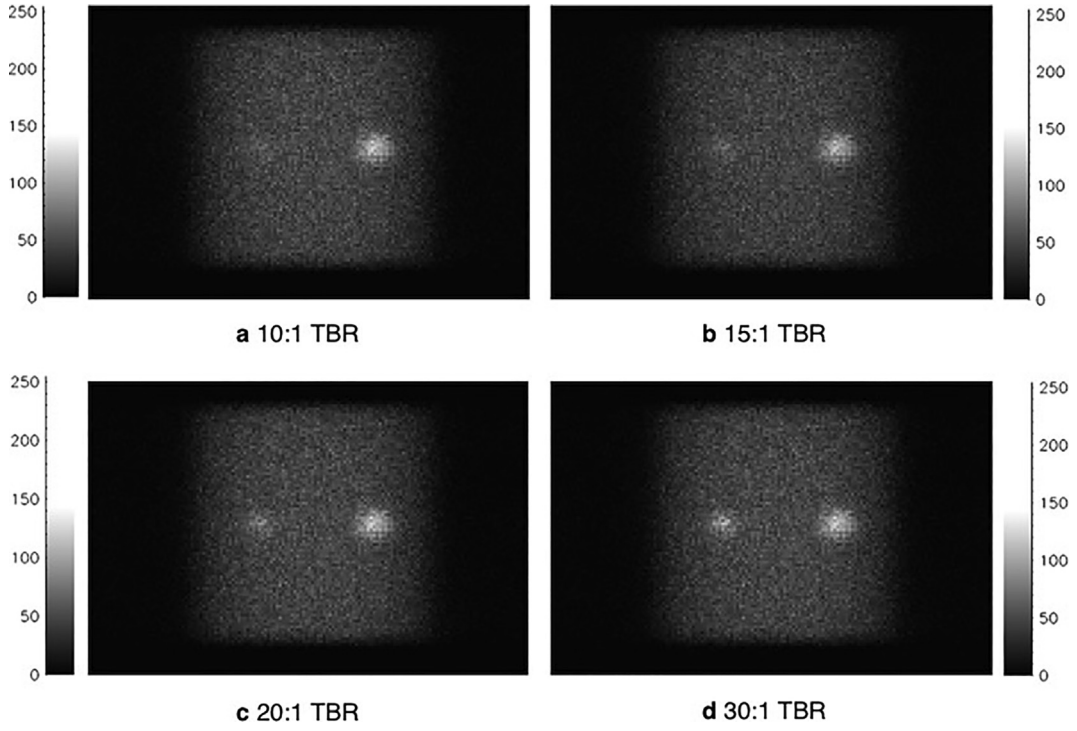

Fig. 4. Reconstructed coronal images of the cylindrical phantom, i.e. in the x-y plane, at different uptakes for the 5 mm. Source. Images were reconstructed using the SAA method. The slice thickness of the reconstruction was set to 1 mm.

Table 1
Image quality metrics for the simulated sources. Reported standard deviation (SD) were calculated by means of error propagation.

TBR	5 mm		10 mm
	IC(%) ± SD	CNR ± SD	CNR ± SD
10:1	32.4 ± 0.3	4.3 ± 0.7	7.3 ± 1.2
15:1	40.2 ± 0.6	5.6 ± 0.8	
20:1	42.5 ± 0.3	6.1 ± 0.9	
30:1	53.7 ± 0.3	10.2 ± 1.6	

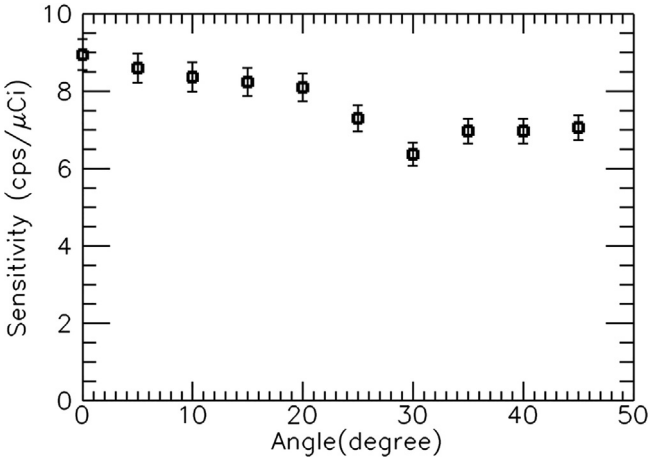

Fig. 5. Sensitivity curve as function of slant angle.

performed matching the simulations, i.e. background and tumor images. The different phantom uptakes were realized changing tumor image acquisition time, proportionally to the requested TBR. Both tumors were centered in the phantom in the z-dimension (perpendicular to the detector face) at a depth from the bottom phantom surface of

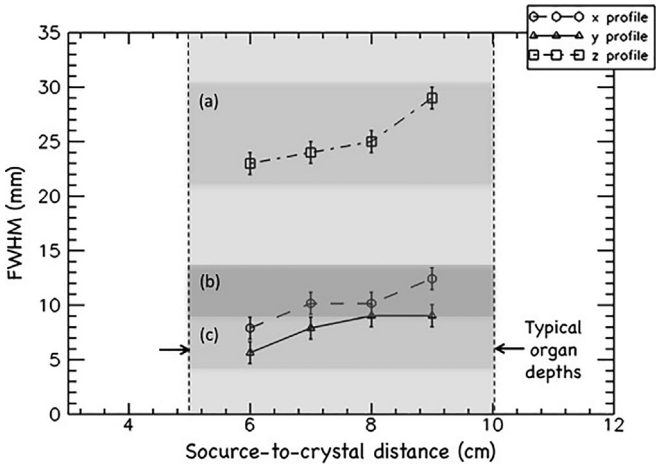

Fig. 6. Spatial resolutions (FWHM) of the reconstructed source as function of the source-to-detector distance. Three spatial resolution bands are indicated: the top one refers to depth resolution (along z) (a), the middle and the bottom ones to x (b) and y (c) resolutions respectively. Error bars take into account the pixel size of the reconstructed image.

3.75 cm. Thus, the simulated tumors were located at a distance of 72 mm from the detector. As described in the previous paragraph, a shift of 30 mm of the collimator-detector system was simulated. The tilting mechanism was simulated with a stepping angle of 3°, i.e. from −45° to +45°; for each projection, 1 min scan time was used to represent clinical acquisitions. The resulted projection images had a matrix size of 150 × 100 pixels. An ensemble of 31 projection datasets was generated and then reconstructed using the SAA method.

Contrast to Noise Ratio (CNR) and Image contrast (IC) were evaluated as function of simulated TBR. The CNR is defined as:

$$CNR = \frac{\bar{x}_S - \bar{x}_{bkg}}{\sigma_{bkg}} \quad (4)$$

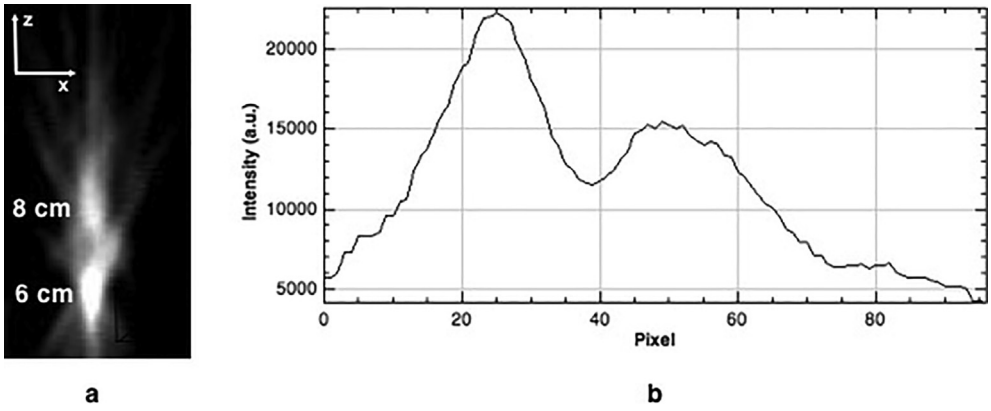

Fig. 7. Reconstructed images of ^{57}Co sources 2 cm apart displayed in the x-z plane (a) and profile plots of image intensities through the sources centers (b). Slice planes are through the lesion centers at approximately 6 cm and 8 cm distance from the crystal.

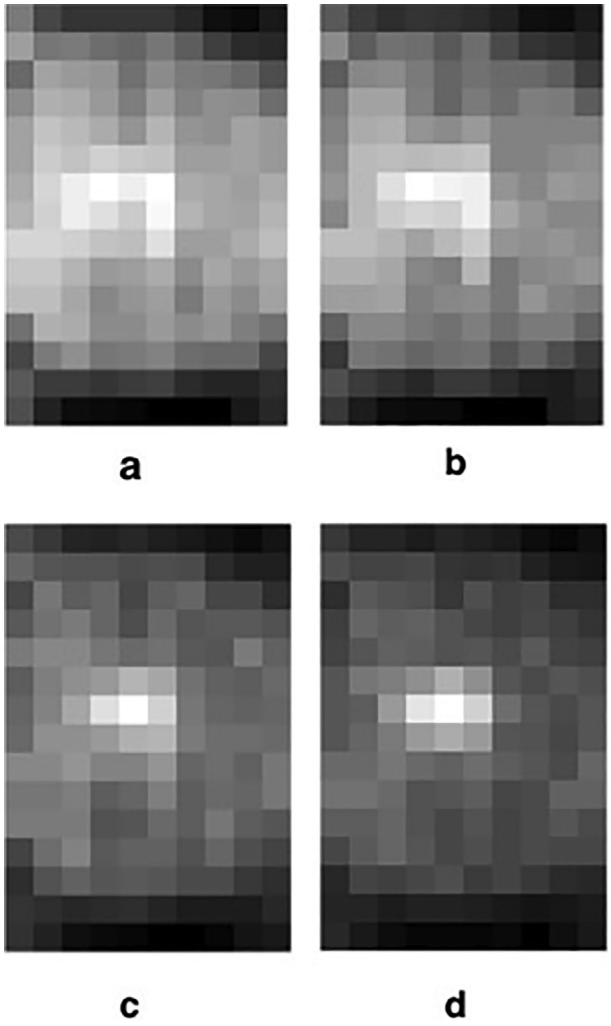

Fig. 8. Reconstructed images, in the x-y plane, of the breast phantom with a radioactivity background for different TBR ((a) 5:1, (b) 10:1, (c) 20:1, (d) 30:1). Each image shows the plane at a distance of 79 mm from the detector where tumor T2 is focused.

The contrast is the difference between the average grey scale of a region of interest (ROI) in the disk ($\bar{x}_S$) and that in an ROI in the background ($\bar{x}_{bkg}$), and the noise can be calculated from the background ROI as well.

The IC due to a small structure of interest is the change in intensity caused by that structure is defined as

$$IC = \frac{\bar{x}_S - \bar{x}_{bkg}}{\bar{x}_{bkg}} \quad (5)$$

where $\bar{x}_S$ is the average signal intensity in the ROI containing tumor, $\bar{x}_{bkg}$ is the average background intensity (in the vicinity of the structure of interest), thus $\bar{x}_S - \bar{x}_{bkg}$ is the change in intensity caused by the lesion or region of interest. In this definition, the IC value theoretically ranges between 0% and 100%.

The lesion's ROI was defined as a circular ROI having a diameter equal to the actual lesion diameter, whilst to get the average background counts an adjacent ROI was used.

Table 2
Image quality metrics for tumors T1 and T2 and different TBR values in the focused x-y plane for GT and planar images. Reported standard deviation (SD) were calculated by means of error propagation.

	TBR	T1		T2	
		IC(%) ± SD	CNR ± SD	IC(%) ± SD	CNR ± SD
GT	5:1	21.8 ± 0.2	3.9 ± 0.3	24.1 ± 0.1	5.6 ± 0.4
	10:1	24.2 ± 0.1	5.8 ± 0.4	28.1 ± 0.1	7.2 ± 0.5
	20:1	28.3 ± 0.1	6.9 ± 0.5	34.7 ± 0.2	8.1 ± 0.8
	30:1	34.9 ± 0.1	7.1 ± 0.6	42.5 ± 0.2	9.8 ± 1.2
Planar	10:1	17.2 ± 0.1	3.7 ± 0.3	18.3 ± 0.1	4.0 ± 0.3

2.4. Experimental equipment and setup

In order to test the VAPHC, the gamma camera GE Millennium (GE Medical Systems-Americas: Milwaukee, WI, USA) was used. Any collimator mounted on the gamma camera was disassembled and removed. The decoy collimator (3-mm thick Plexiglas) supplied by the manufacturer was placed on the gamma camera to both provide a resting base for the collimation system and to ensure the electrical connection with the acquisition system. In this configuration, an air gap of approximately 12 mm remains between the decoy collimator and the scintillation crystal, thus the distance between the collimator top and the crystal top is approximately 61 mm. Both the collimator case and the detector area not covered by the collimator were completely shielded: the inside of the collimator case was shielded with lead slices and an adequate lead shield was placed around the detector to prevent the penetration of direct radiation from the source. Inadequate shielding might cause unwanted detected counts as the detector area not covered by the collimator would also be active. The VAPHC was placed at the centre of the 36 cm × 51 cm gamma camera head, thus all image acquisitions were performed within the gamma camera central

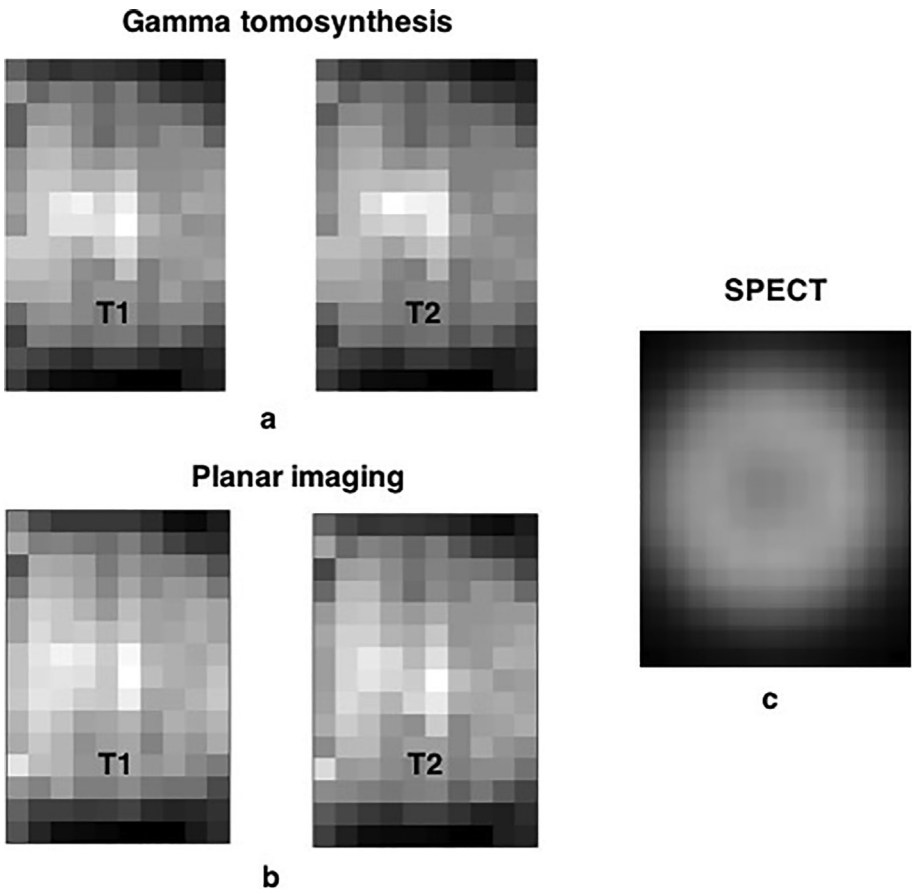

Fig. 9. Breast phantom (10:1 TBR) reconstructed images, in the x-y plane, where tumors are focused: GT images (SAA reconstruction) (a), planar images (b) and circular orbit SPECT (OSEM reconstruction) (c).

FOV.

2.4.1. Sensitivity and spatial resolution

A preliminary characterisation in terms of sensitivity was performed using a ^{99m}Tc disk source containing approximately 2 mCi of ^{99m}Tc solution. Acquisitions were performed by tilting the collimation system in step of 5°, with an acquisition time of 30 s per slant angle, an energy window width of 20% centred at 140 keV and a matrix size of 512 × 512. The experimental points for the sensitivity curve were obtained dividing the source counts registered in each projection image at different angles by the source activity.

System spatial resolutions in planar (x-y plane) and depth direction (along z) were measured using a 46 μCi ^{57}Co (122 keV, 85% BR, emission) point source (1.5 mm diameter). All acquisitions were performed by tilting the collimation system in step of 5° and the acquisition time was set at 5 min for each planar projection image. The total number of counts registered by the system was not fixed as they depend on the slant angle, but an average of approximately 300 k counts was achieved for each projection image. Using an energy window width of 20%, centred at 122 keV and a matrix size of 512 × 512, a count rate between 300 and 500 counts per second was generated. The source was placed at 0 cm, 1 cm, 2 cm and 3 cm from the collimator to study the resolution capabilities of the system in detecting lesions placed at different depths inside the organ to be examined. For the source-to-collimator distances of 1 and 2 cm, a relative shift of 2 cm between the source and the collimator has to be provided, while when the source-to-collimator distance becomes 3 cm the provided shift has to be 3 cm. In this way, the source has never remained outside the collimator FOV at all slant angles. In our case, for convenience, the source was moved respect to the collimation system and not viceversa.

To better evaluate the resolution in the depth direction (along z axis), two ^{57}Co point sources were imaged gradually reducing the distance between them until the two sources cannot be separated in the reconstructed image. Acquisition details include an energy window width of 20% centred at 122 keV, a matrix size of 512 × 512, a 5° rotation step, an acquisition time of 5 min for each planar projection image and a relative shift of 2 cm between the sources and the collimator.

2.4.2. Breast phantom

As the proposed system was designed to detect lesion smaller than 1 cm in superficial organs (i.e., with application in breast or cardiac imaging), a breast phantom was realised. The breast phantom is homemade plastic cylinder [22] (6.2 cm in diameter and 15 cm in height) filled with tecnetiated water up to 4 cm in height to simulate the breast compression thickness. The phantom contains one commercially available fillable point marker source simulating a tumour lesion. The marker source is a small clear plastic cylindrical receptacles, 2.54 cm in diameter × 1.27 cm thick, with a spherical centred channel to contain the radionuclide. Only the internal cavity of 4 mm diameter can be filled by 0.2 ml of the radionuclide, thus reproducing a lesion size smaller than 1 cm. In order to simulate the activity in the breast expected in clinical scans, the outer cylinder was filled with ^{99m}Tc solution to obtain a TBR ranging from 5:1 to 30:1. For realizing the 10:1 TBR, the radioactivity concentrations were approximately 1 μCi/ml (37 kBq/ml) and 100 nCi/ml (3.7 kBq/ml) for lesions and background respectively, while for the other configurations the tumor's activities were scaled accordingly. The source was suspended inside the cylinder at two different distances from the collimator (15 mm and 35 mm), as shown in Fig. 3. From here, we will refer to T1 to denote the tumor

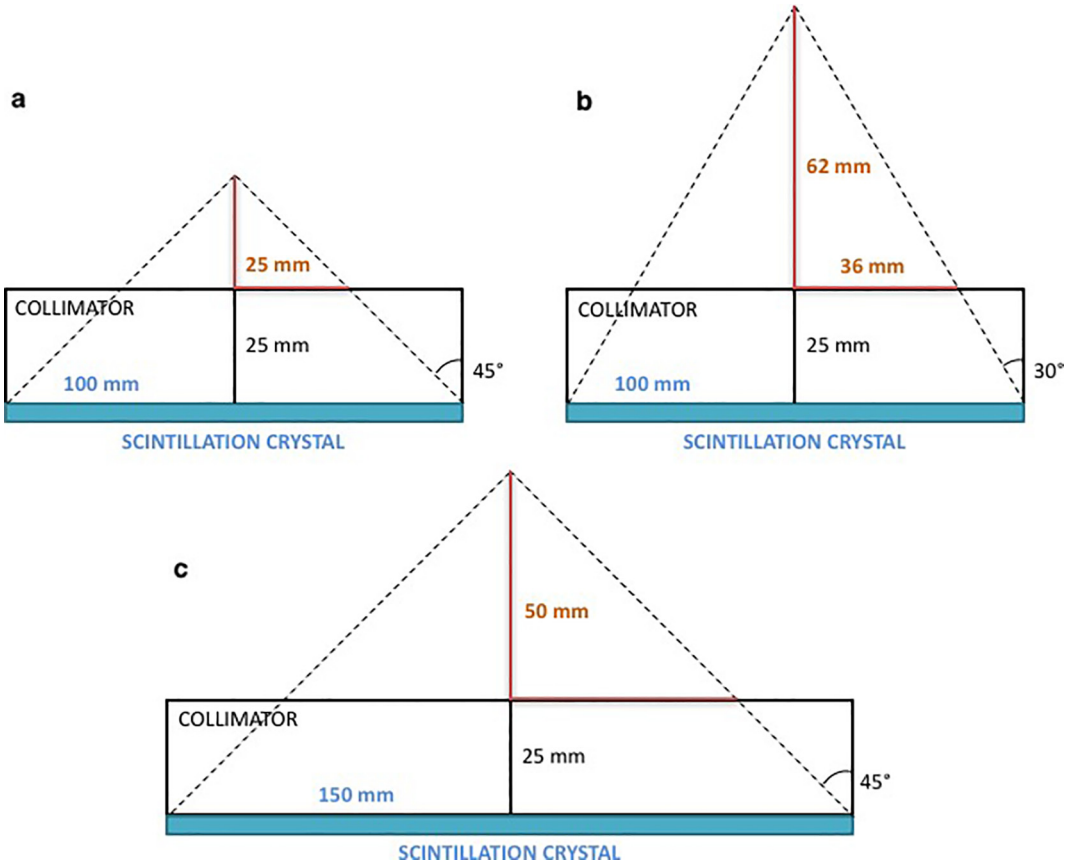

Fig. 10. Schematic representation of the VAPHC's field-of-view.

Table 3
Evaluation of radiation leakage between the collimation elements for different slant angles.

Slant angle	Radiation leakage (%)
0°	0
5°	0
10°	17
15°	0
20°	1
25°	1
30°	22
35°	6
42°	7
45°	16

located at a greater distance from the collimator and to T2 to indicate the other one.

In order to ensure a FOV large enough to cover the whole phantom at all slant angles, a dynamic shift was implemented: the phantom was shifted by 4 cm in the ranges $[-45°, -25°] \vee [+25°, +45°]$ and by 2 cm in the ranges $[-20°, -5°] \vee [+5°, +20°]$. These phantom shifts were provided for all slant angles other than zero. 19 projection data with an acquisition time of 30 s per slant angle were acquired by tilting the collimation system in step of 5° over 90° (i.e., in the range $[-45°, +45°]$). Acquisition parameters included a 128 × 128 projection matrix (4.52 mm pixel size) and 20% wide energy window. In the present study, the acquired count density with the breast phantom was approximately 90 counts/cm^2 for each planar projection image, resulting in approximately 1700 counts/cm^2 for 10 min acquisition.

Contrast to Noise Ratio (CNR) and Image contrast (IC) were evaluated for both sources and different TBR. Circular ROIs were selected within the lesions by setting ROIs diameter equal to the diameter at the FWHM of the lesion signal, as determined from a signal profile through the lesion center. This corresponded to ROI diameter of approximately 12 mm. Background ROIs had the same diameter, and their center were placed approximately 16 mm from the center of the lesion.

GT imaging results of the breast phantom with TBR 10:1 were compared to planar images of equal scan-time. Reconstructed GT images were also compared to SPECT images of a source placed at the center of the cylinder (TBR 10:1). Data were acquired using both heads of the SPECT system and the associated parallel beam LEHR collimator (hole length = 35 mm, hexagonal hole size = 1.5 mm, septal thickness = 0.2 mm) with the cylinder axis perpendicular to the patient table. Images were acquired using a 128 × 128 projection matrix, 32 angular views over 360° with an acquisition time of 20 s/view and a Radius of Rotation (ROR) of 19 cm. Total acquisition time was approximately 10 min; reconstruction was performed using the OSEM iterative reconstruction (8 iterations, 8 subsets).

3. Results

3.1. Monte Carlo simulation results

The reconstructed images of the simulated phantom are reported in the following. Fig. 4 shows the images of the reconstructed phantom (150 × 100 mm^2) in the x-y plane for the 5 mm source at different TBR; the 10 mm source TBR is 10:1. Table 1 summarizes the results of the simulation study for both tumors and different TBR values. As expected, the images with higher TBR are superior in terms of both IC and CNR.

3.2. Sensitivity and spatial resolution

The sensitivity curve is shown in Fig. 5. The measured sensitivity decreased from approximately 9 cps/μCi to 6 cps/μCi varying the slant

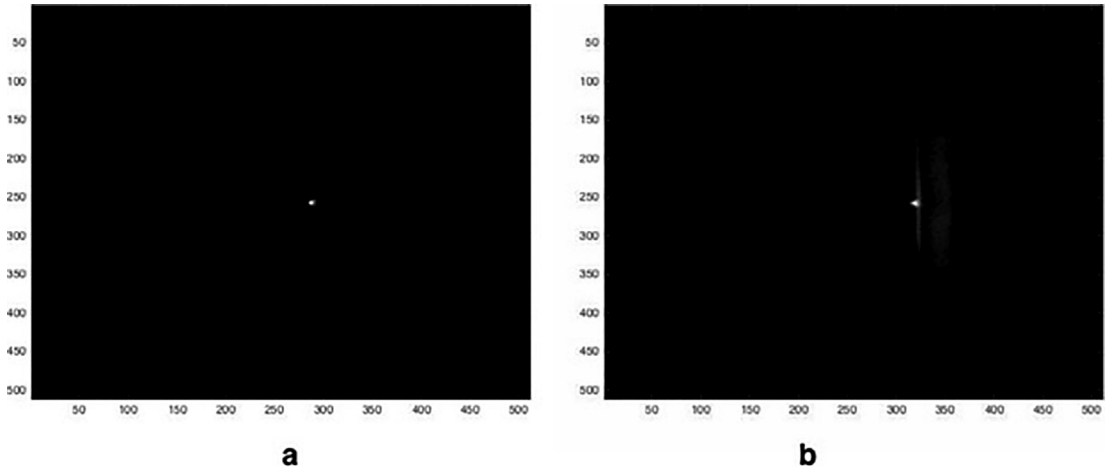

Fig. 11. Planar projection images of ^{57}Co point source at 0° (a) and 30° (b) where the radiation leakage is visible.

angle from 5° to 45°. The experimental error associated are calculated by means of error propagation considering a standard deviation on the number of counts given by the Poisson statistics. Unlike the design that uses the Moore approach, the collimator hole geometry is fixed here; the theoretical sensitivity should be constant with slant angles for this collimator design. However, the experimental sensitivity decreases for angles higher than 25°; this phenomenon is compatible with the count loss between the collimation modules.

Spatial resolutions are obtained as FWHMs of the 3D reconstructed source profiles by using a Gaussian function within ImageJ (NIH, Bethesda, MD, USA) curve fitting application. FWHM values are reported in Fig. 6 along x, y, z directions for different source-to-detector distance. Given the small source size compared to the measured FWHM values, the source dimension was not deconvolved from the measured FWHMs.

To better evaluate the imaging performance of the system in depth direction (z axis), Fig. 7 shows the reconstructed images of ^{57}Co sources 2 cm apart displayed in the x-z plane and the profile plots of image intensities through the sources centers. These latter profiles demonstrate that two point sources 2 cm apart can be separated in the reconstructed image.

3.3. Breast phantom results

To quantitatively analyse the results of reconstructed breast phantom images, tumors IC and CNR for different TBR are reported in the following. For the sake of simplicity, the coronal reconstructed images in T2 focused plane will be presented (Fig. 8), whilst the results for tumor T1 will be reported in terms of imaging parameters only.

Table 2 summarises the IC and CNR resulted from GT and planar imaging (TBR 10:1) for the experimental breast phantom tumors and different TBR values. The results confirm the advantage of GT in this regard for both tumors. GT CNR values for T2 are over visibility limit for all studied TBR (Rose criterion) [22]. Increasing the uptakes, CNR values become apart and, as expected, these values are higher for tumor T2 which is closer to collimator than tumor T1.

Fig. 9 illustrates the GT breast phantom images (10:1 TBR) in the focused x-y plane for tumors T1 and T2, the planar images and that obtained with circular-orbit acquisition SPECT (the lesion was not detectable). The cold circle visible in the SPECT images is the plastic casing of the point marker source. The differences in visibility of the point source plastic casing are due to the partial volume effects (PVEs). The magnitude of these effects depends mainly on the size of the object of interest in relation to the spatial resolution of the system, thus affecting the results of VAPHC GT and planar imaging compared to SPECT. The spatial resolution of SPECT system, which is limited by the ROR, leads to a blurring of the reconstructed image. As a consequence, activity from a source distribution will be spread out over a volume in the reconstructed image; this results in a variation of apparent activity concentration. Obviously, the impact of the PVE is more prominent when small objects are of interest. Therefore, in SPECT imaging, PVEs hinders the visibility of the 4-mm source that has a diameter less than two-three times the FWHM of the imaging system. This does not happen in GT and planar images with VAPHC where the higher spatial resolution due to the reduced object-to-detector distance limits the PVEs increasing the small lesion visibility. Moreover, the difference between VAPHC GT and SPECT images is even more marked due to the different uniformity/reconstruction methods. The SPECT system has better image uniformity compared to VAPCH system as well as the OSEM reconstruction method is more refined than SAA algorithm used in GT. These latter elements contribute to have differences in visibility of the radioactive and non-radioactive distribution.

4. Discussion

The GT reconstruction results of simple objects demonstrated that the system is able to correctly reconstruct the shape of a phantom and to properly identify the depth position of two objects, i.e., the tumor lesions, separately. The present study demonstrated that GT makes possible to obtain a high imaging improvement compared to SPECT, where the spatial resolution/sensitivity trade-off is always limited by the ring size. The high spatial resolution achievable with the VAPHC prototype demonstrates the system feasibility in the detection and localisation of sub-centimetre lesions. The proposed device represents a possible solution for an imaging system aimed at small organs, for example breast, head and thyroid or for detecting superficial lesions. The system works in patient proximity to detect lesions placed at a distance that varies from 0 to 8 cm from the surface of the examined object. The VAPHC has the attractive feature of being composed by single collimation modules. Differently from other proposed systems where plates are sheared one above the others, this design allows to implement slant angles higher than 30°.

The spatial resolution/sensitivity trade-off with the proposed approach can be compared with the design that uses the Moore methodology. The VAPHC sensitivity remains constant with the slant angles, as the hole geometry does not vary when the slant configuration is created. Differently, the design that uses the Moore approach produces a decrease in sensitivity with a $\cos^3(\theta)$ factor, because the effective collimator hole diameter decreases and hole length increases. This behavior improves the collimator spatial resolution (by $\cos(\theta)$ factor) in the slant dimension at the expense of sensitivity. Using VAPHC, spatial resolution in the slant dimension becomes worse (by $1/\cos(\theta)$ factor) as

the effective object dimension results magnified along the slant direction due to how gamma rays are backprojected along non zero angles. The spatial resolution in the non-slant dimension is constant with both approaches but the VAPHC, incorporating larger slant angles, allows to improve reconstructed spatial resolution in the depth dimension. The slant mechanism based on the Moore approach limits the collimator slant angle within a range of ± 25°; incorporating larger slant angles is very difficult as the hole diameter should be adjusted to match the registration of the plates. However, imaging a FOV over a higher range of slant angles, as happens with VAPHC, expands the slant dimension over which the detector must be positioned. This can be achieved either by translating the detector laterally with slant angle or by using a larger detector in the lateral dimension.

The reconstruction volume in the VAPHC working range [−45°; +45°] can be defined from simple geometric considerations. The effective FOV over all slant angles is reduced in the slant dimension and depends on the collimation length in the slant dimension. As represented in Fig. 10(a), being the collimation length of 6 cm in the slant dimension, for a shift of the collimation system of 2 cm and 45° slant angle, the triangular FOV has 5 cm base and 2.5 cm height. Repeating the same considerations, for a 2 cm shift and 30° slant angle, the triangular FOV has 7.2 cm base and 6.2 cm height (Fig. 10(b)). For imaging larger object sizes, the collimation length in the slant direction has to be increased. This can be achieved increasing the number of collimation elements or providing a relative shift between the collimation system and the object. With the actual collimation length in the slant dimension, that is limited to 6 cm, a relative shift between the collimation system and the object has to be implemented. For example, increasing the shift to 4.5 cm for the slant angle of 45° (Fig. 10(c)), the triangular FOV increases the base to 10 cm and the height to 5 cm.

These considerations allow to demonstrate the concept of the so-called adaptivity, which is the ability to adapt the acquisition depending on clinical needs: varying the slant angles and translation parameters allows to modify the FOV of the acquisition. Moreover, depending on the position and size of the object of interest, the acquisition system will adapt it by acting on different acquisition parameters, such as number of projections angles or acquisition time. Differently from the conventional SPECT, the acquisition can be performed by increasing the number of views focusing onto a particular object with the aim to help the diagnosis.

Despite of these advantages, some system criticalities have to be considered. On one hand, the collimator segmentation, even if necessary, induces leakage of gammas between collimation modules causing unwanted detected counts. Table 3 reports an evaluation of the percentage of leakage between the collimation modules for different slant angles. Fig. 11 shows the comparison between planar projection images of ^{57}Co point source at 0° where radiation leakage is not present and at 30° where radiation leakage between adjacent collimation elements causes unwanted detected counts. On the other hand, some planar projection images could be affected by a count loss phenomenon corresponding to the area where the shielding action of the lead plates between the collimation elements should attenuate the radiation source. This latter effect could be limited by reducing the lead thickness between each collimation element or using material different from lead, i.e. gold or tungsten. The non-perfect shielding of the inner collimator case sides could cause counting losses at the edges of the collimator. This disadvantage could be solved introducing a mobile shielding system inside the collimator case that follows the collimation elements in their tilting movement, i.e. with two lead wings anchored to the collimator, or increasing the collimation area with more collimation modules. Moreover, spatial resolution results of VAPHC are worsened by the presence of empty spaces between the collimation blocks and the lower and upper sides of the collimator case. Despite the empty space between the collimation blocks and the lower side of the collimator case is required for allowing the modules to tilt and cannot be reduced, the space above the collimation elements can be reduced optimizing the mechanics that allows the rotation movement. At the same time, using a dedicated gamma camera allows to reduce the space occupied by the decoy collimator of the clinical gamma camera and the empty space between the decoy and the top of the scintillation crystal.

Feasibility studies on the collimator showed that it is better to realise a collimator with a single slant direction. Since the resolution in the coronal plane is worse in the slant direction, a method for improving lesions detection capability could be mounting the collimator on a rotating support to perform a double acquisition, i.e., with x or y as slant direction respectively. Moreover, to solve the problem of the worst spatial resolution in depth direction, it could be possible to implement an acquisition system with two heads supplied by the slant collimator, in configuration 0–180° or 0–90°. In particular, in the latter configuration the depth direction for the 0° head would correspond to a coronal direction for the 90° head, thereby further improving spatial resolution results.

5. Conclusions

A novel collimation system based on variable tilt-angle parallel-hole collimation modules has been tested to perform tomographic imaging in nuclear medicine. The measures carried out and the employment conditions offer a broad view of the potential of this new apparatus: it demonstrated the potential for superior spatial resolution, IC and CNR compared to planar and SPECT acquisitions. This could result in a substantial improvement of diagnostic ability in particular for lesions placed in the vicinity of the patient's skin. Without using a detector orbiting motion, the patient-to-detector distance can be minimised as the device can be placed in contact with the organ to be examined. This feature results in high spatial resolution and allows to image critical regions. The VAPHC for GT could be mounted on a conventional gamma camera dedicated to small organ imaging relatively inexpensively and could be made available either as an accessory at the time of scanner installation or as an optional add-on at a later date. This system could represent a possible improvement in collimator design and in image acquisition modality and could help clinicians in detecting lesions at the bedside, where portable and simpler systems, as those presented, may be adequate. All these characteristics could make the device particularly useful in case of patients who are often unable or unwilling to cooperate. Despite these advantages, in vivo applications require further studies to be employed on both collimation design, acquisition and reconstruction method. Our experience indicates that the presented collimation system could represent in the near future an important advance in developing devices dedicated to imaging of small lesions, without the need to rotate the system around the patient's body but adapting the acquisition to clinical needs.

Declaration of Competing Interest

The authors declare that they have no known competing financial interests or personal relationships that could have appeared to influence the work reported in this paper.

References

[1] Majewski S, Kieper D, Curran E, et al. Optimisation of dedicated scintimammography procedure using detector prototypes and compressible phantoms. IEEE Trans Nucl Sci 2001;48(3):822–9.
[2] More MJ, Goodale PJ, Majewski S, Williams MB. Evaluation of gamma cameras for use in dedicated breast imaging. IEEE Trans Nucl Sci 2006;53(5):2675–9.
[3] Pani R, Bennati P, Cinti MN, et al. Imaging characteristics comparison of compact pixellated detectors for scintimammography. Nucl Sci Symp Conf Record 2004;6:3748–51.
[4] Stebel L, Carrato S, Cautero G, et al. A modular prototype detector for scintimammography imaging. Nucl Sci Symp Conf Rec 2005;5:3027–31.
[5] Brzymialkiewicz CN, Tornai MP, McKinley RL, Bowsher JE. Evaluation of fully 3-d emission mammotomography with a compact cadmium zinc telluride detector. IEEE Trans Med Imaging 2005;24(7):868–77.
[6] Tornai MP, Bowsher JE, Jaszczak RJ, et al. Mammotomography with pinhole

incomplete circular orbit SPECT. J Nucl Med 2003;44:583–93.
[7] Giokaris ND, Loudos GK, Maintas D, Papapanagiotou D, Nikita KS, Uzunoglu NK, et al. Imaging of breast phantoms using a high-resolution position sensitive photomultiplier tube. Nucl Instr Meth Phys Res 2003;497(1):141–9.
[8] Dale S, Edholm PE, Hellstrom LG, Larsson S. Ectomography – a tomographic method for gamma camera imaging. Phys Med Biol 1984;30(11):1237–49.
[9] Xu J, Liu C, Wang Y, Frey EC, Tsui BMW. Quantitative rotating multisegment slant-hole SPECT mammography with attenuation and collimator-detector response compensation. IEEE Trans Med Imaging 2007;26(7).
[10] Moore RH, Alpert NM, Strauss HW. A variable angle slant-hole collimator. J Nucl Med 1983;24:61–5.
[11] Gopan O, Gilland D, Weisenberger A, Kross B, Welch B. Molecular imaging of the breast using a variable-angle slant-hole collimator. IEEE Trans Nucl Sci 2014;61(3):1143–52.
[12] Gilland DR, Welch BL, Lee S, Kross B, Weisenberger AG. Evaluation of a novel collimator for molecular breast tomosynthesis. Med Phys 2017;44(11):5740–8.
[13] Pellegrini R, Pani R, Cinti MN, Longo M, Lo Meo S, Viviano M. Gamma emission tomosynthesis based on an automated slant-hole collimation system. J Inst 2015;10:C03003.
[14] A tilting collimator, in particular for single-photon emission computed tomography. United States Patent US9362013B2. KAY SYSTEMS ITALIA S.r.l., Rome (Italy). Università degli Studi di Roma La Sapienza (Rome, Italy).
[15] http://www.ksi.it/?page_id=1812&lang=en.
[16] Dobbins III JT, Godfrey DJ. Digital x-ray tomosynthesis: current state of the art and clinical potential. Phys Med Biol 2003;48:R65–106.
[17] Gomi T, Hirano H, Nakajima M, Umeda T. X-ray digital linear tomosynthesis imaging. J Biomed Sci Eng 2011;4:443–53.
[18] Chen Y, Balla II A, Rayford CE, Zhou W, Fang J, Cong L. Digital tomosynthesis parallel imaging computational analysis with Shift and Add and Back Projection reconstruction algorithms. Int J Comput Biol Drug Des 2010;3(4):287–96.
[19] Niklason LT, Christian BT, Niklason LE, et al. Digital tomosynthesis in breast imaging. Radiol 1997;205:399–406.
[20] Cherry SR, Phelps ME, Sorenson JA. Physics in nuclear medicine. Philadelphia: Saunders; 2003.
[21] Mann SD, Perez KL, McCracken EKE, Shah JP, Wong TZ, Tornai MP. Initial in-vivo quantification of Tc-99 m Sestamibi uptake as a function of tissue type in healthy breasts using dedicated breast SPECT-CT. J Oncol 2012:7.
[22] Cinti MN, Pani R, Pellegrini R, Bonifazzi C, Scafè R, De Vincentis G, et al. Tumor SNR analysis in scintimammography by dedicated high contrast imager. IEEE Trans Nucl Sci 2003;50(5):1618–23.